

SYNTHESIS, THERMAL, ELECTRICAL AND MAGNETIC PROPERTIES OF $\text{Bi}_{0.6-x}\text{Mn}_{0.5}\text{Ni}_{0.5}\text{Fe}_2\text{O}_4$ FERRITE

M. ALI^{a*}, M. AKRAM^b, S. M. ZAFAR IQBAL^c, M. ASHFAQ^a

^aDepartment of Chemistry, The Islamia University of Bahawalpur, 63100, Pakistan

^bDepartment of Educational Training, The Islamia University of Bahawalpur, 63100, Pakistan

^cDepartment of Electrical Engineering, Khawaja Fareed University of Engineering and Information Technology, Rahim Yar Khan, Pakistan

A series consisting of six samples of $\text{Bi}_{0.6-x}\text{Mn}_{0.5}\text{Ni}_{0.5}\text{Fe}_2\text{O}_4$ spinel ferrites with different molar concentrations have been fabricated by using the facile co-precipitation method. ($x=0.0, 0.10, 0.20, 0.30, 0.40$ and 0.50). The synthesized series structural properties and phase information are studied using XRD. FESEM is used to explore the surface morphology and EDS is used to characterize the composition of elements in the nanoparticles. Raman Spectroscopy of the synthesized samples confirms the five Raman active bands Raman spectra i.e. A_{1g} , E_g , and three belongs to T_{2g} . These five peaks are at $200, 318, 477, 560,$ and 684 cm^{-1} indicates the successful confirms the formation of $\text{Bi}_{0.6-x}\text{Mn}_{0.5}\text{Ni}_{0.5}\text{Fe}_2\text{O}_4$ cubic nanoparticles. The vibrating sample shows a superparamagnetic character in magnetometry measurements. As the concentration of Bi is increased the saturation magnetization decreases from the value 82 emu/g . The graphs of TGA and DTA analysis showed weight losses with the rise in temperatures but no further weight loss was observed after 800°C and limits at 950°C . The dielectric measurements were performed between frequency ranges of 1MHz to 3GHz of the applied electric field. The dielectric parameters were observed to decrease by Bi substitutions whereas the particle size increases. This decreasing effect remains to continue by increasing the frequency. However, the resistance of the nanocomposite material is found to decrease. These dielectric parameters suggest that these nanocrystalline ferrites with the domino effect are suitable for microwave devices of GHz frequencies ranges.

(Received February 4, 2020; Accepted May 22, 2020)

Keywords: Spinel ferrites, Magnetic properties, Co-precipitation method, X-ray diffraction

1. Introduction

The spinel ferrites have got great interest in advanced scientific and technological instruments where these ferrites materials have vast applications such as magnets, catalysts, a variety of sensors, phase shifters, insulators, etc. [1-5]. These materials also play a key role due to remarkable properties in several electrical applications such as power transformers, recording instruments, electric generators, and motors, storage devices in a computer, microwave instruments [6]. These magnetic materials show peculiar characteristics owing to their cation distribution in the structure, large electrical resistivity and very low dielectric loss and little conductivity [7-8]. These attributes are also related to their synthesis techniques, chemical composition [9]. They exhibit high specific resistance and flexible behavior for the modifications of their magnetic properties.

In recent decades, nano ferrite materials have shown a little bit hysteresis loss compare to conventionally synthesized ferrites which is a promising character for high-frequency magnetic devices. These nano ferrite materials also show unusual magnetic behavior such as even their saturation magnetization decreases but they show enhanced coercivity character [10]. These nano-ferrite materials are also used in the removal by adsorbing toxic heavy metals such as Pb, Cd, Cr, Co & As [11]. These nanomaterials have been used as catalysts and photocatalytic for the

* Corresponding author: muradali70@yahoo.com

degradation of organic dyes which are pollutants under visible light [12,13]. The nano ferrite materials are also used in the inductive components of electric appliances. Due to the phenomenon of electrons scattering at the grain boundary in nano ferrite materials their eddy current losses are reduced in electric devices [14].

These ferrite materials are synthesized by a solid-state method that is utilized for bulk synthesis and requires high temperatures ($>1000\text{ }^{\circ}\text{C}$). In this method reaction kinetics is slow and the size of the product remains in the micrometer regime due to agglomeration [15]. The solid-state synthesis method with these drawbacks attracted the researchers towards other soft chemical synthesis routes which are becoming popular among scientists around the globe. The yield of these ferrite nanoparticles shows good attributes for the desired stoichiometry and greater control on composition.

In this perspective, different synthesis routes to produce nano-ferrites have been employed such as co-precipitation technique, sol-gel technique, the hydrothermal technique to achieve the desired stoichiometry. These techniques are considered a low-temperature synthesis technique for the nano ferrite materials [16]. The overall properties of these nanoparticles strongly depend on temperature, synthesis technique, ionic size of the dopant and cation distribution. The literature suggests that the Bi doping can change the attributes of $\text{MnNiFe}_2\text{O}_4$ nanoparticles, and their magnetic, dielectric and electrical properties could be improved.

In this work, the impacts of Bi substituted $\text{MnNiFe}_2\text{O}_4$ ferrites nanoparticles series have been synthesized by applying the co-precipitation procedure. The strategy is considered economical course to get the specified compositions of Bi substituted $\text{MnNiFe}_2\text{O}_4$ nanoparticles with distinctive stoichiometric proportions i.e. $\text{Bi}_{0.6-x}\text{Mn}_{0.5}\text{Ni}_{0.5}\text{Fe}_2\text{O}_4$ ($x = 0.0, 0.10, 0.20, 0.30, 0.40, 0.50$).

2. Method and materials

The metal-based chemicals used in the synthesis are listed below:

Materials	Company
$\text{Ni}(\text{NO}_3)_2 \cdot 6\text{H}_2\text{O}$	BDH, 98% purity
$\text{Mn}(\text{CH}_3\text{CO}_2)_2 \cdot 4\text{H}_2\text{O}$	Sigma, 98% purity
$\text{Fe}(\text{NO}_3)_3 \cdot 9\text{H}_2\text{O}$	Merck, 98% purity
NaOH	Sigma, 99% purity Merck,
$\text{Bi}(\text{NO}_3)_3 \cdot 5\text{H}_2\text{O}$	99% purity

2.1. Synthesis technique

The ferrites nanoparticles of various compositions i.e. $\text{Bi}_{0.6-x}\text{Mn}_{0.5}\text{Ni}_{0.5}\text{Fe}_2\text{O}_4$ ($x = 0.0, 0.10, 0.20, 0.30, 0.40, 0.50$) were prepared by mixing the aqueous solutions in the required stoichiometric ratio (100 ml each) of metal salts whose molar quantities [$0.2\text{M Fe}(\text{NO}_3)_3$, $0.1\text{M Ni}(\text{NO}_3)_2$, $0.1\text{M Mn}(\text{CH}_3\text{COO})_2$] using deionized water. The solutions of Bismuth nitrate were prepared by adding a few drops of Nitric acid until the pH of the solution is between 3-4. The mixed solutions were stirred at $65\text{ }^{\circ}\text{C}$ to get a uniform sample solution then their pH was adjusted to about 11-12 by adding freshly prepared 2M aqueous solution of Sodium Hydroxide dropwise. Each resultant sample was further stirred for 6 hours and before left overnight. Then the precipitates obtained after filtration were washed many times with a mixture of deionized warm water and ethanol until the pH of the washing was reduced to ~ 7 . Drying of precipitates was carried out in the oven at $100\text{ }^{\circ}\text{C}$ for 2 hours. Then precipitates were ground after drying in the oven and then heated at $950\text{ }^{\circ}\text{C}$ using Muffle Furnace.

2.2. Characterization techniques

The $\text{Bi}_{0.6-x}\text{Mn}_{0.5}\text{Ni}_{0.5}\text{Fe}_2\text{O}_4$ synthesized nanocrystals series structural properties were characterized by XRD (X-ray Diffraction) technique. The surface properties and morphology of the synthesized series were explored by FESEM (Field emission scanning electron microscopy),

and the elemental makeup of the synthesized series samples was established by using EDS (energy dispersive spectroscopy). The Raman Spectroscopy of the synthesized series samples was performed to confirm the cubic spinel structure of ferrites. The materials are also characterized by TGA (Thermogravimetric analysis) and DTA (Differential thermal analysis) to determine the mass loss or gain during decomposition or oxidation process synthesized series samples. The dielectric measurements were performed to check the electrical resistivity of the synthesized series. The magnetic study of the synthesized series was performed by using VSM (Vibrating Sample Magnetometer) at room temperature.

3. Results and discussion

3.1. Structural analysis using xrd diffraction

The structural properties of the synthesized $\text{Bi}_{0.6-x}\text{Mn}_{0.5}\text{Ni}_{0.5}\text{Fe}_2\text{O}_4$ ferrites series were deduced using XRD. Fig. 1 showed the comparison between series of $\text{Bi}_{0.6-x}\text{Mn}_{0.5}\text{Ni}_{0.5}\text{Fe}_2\text{O}_4$ ($x = 0.0, 0.10, 0.20, 0.30, 0.40, 0.50$) ferrite nanoparticles, of various compositions. The samples series XRD peaks patterns illustrate the typical character of a cubic spinel structure with single-phase, while the intensities of peaks indicate a degree of crystallinity of prepared samples is high. From the results of the XRD peaks calculated lattice planes belong to (220), (311), (222), (400), (422), (511) and (440) which confirms the spinel cubic structure with the $\text{Fd}\bar{3}\text{m}$ space group symmetry [17]. The lattice planes in the XRD patterns for all samples of the series agree well with the powder diffraction of the spinel cubic structure of the JCPDS file (card no.072-2082) [18]. The strong peaks indicate the size of the samples grain is fine [19].

The particle sizes (D) were calculated from the diffraction peak 311 using the following Scherrer's equation:

$$D = \frac{k \lambda}{\beta \cos\theta} \quad (1)$$

where D = Crystallite size, θ = Bragg angle, λ = wavelength of X-ray radiation, and β = Full width at half maximum (FWHM).

The calculated mean diameter (D) of these samples is nearly the same ranging from 25-35 nm as shown in Table (1). The literature recommends that the crystallite measure of nanoparticles less than 50 nm is more successful in switching applications due to excellent signal-to-noise proportion [20]. The lattice constant 'a' is calculated by the following formula;

$$\frac{1}{d^2} = \frac{h^2+k^2+l^2}{a^2} \quad (2)$$

where, d = inter-atomic spacing, a = lattice constant.

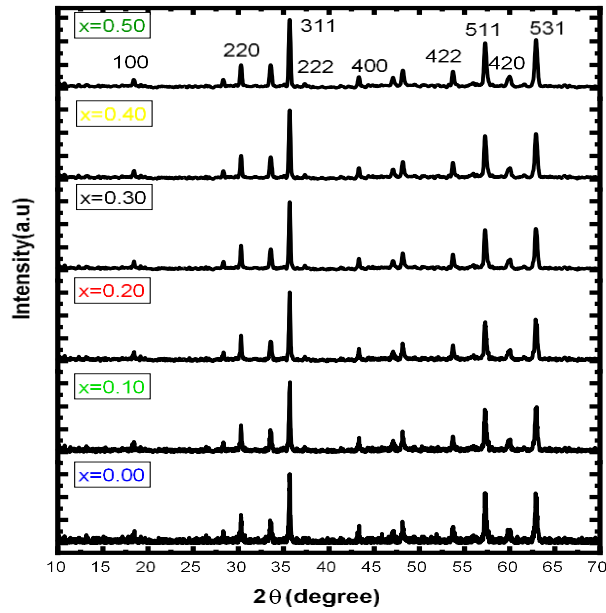


Fig.1. XRD patterns of series of $\text{Bi}_{0.6-x}\text{Mn}_{0.5}\text{Ni}_{0.5}\text{Fe}_2\text{O}_4$ nanoparticles.

The calculated lattice constant of $\text{Bi}_{0.6-x}\text{Mn}_{0.5}\text{Ni}_{0.5}\text{Fe}_2\text{O}_4$ series also given in Table (1), and their values suggested that by the increase in ' Bi^{2+} ' concentration, the lattice parameter will also increase as suggested in the literature [21–24]. The samples X-ray density was calculated using the following equation and expressed in Table (1) [25].

$$\rho_{\text{X-ray}} = \frac{nM}{N_A V_{\text{cell}}} \quad (3)$$

where, n = No. of atom per unit cell, $\rho_{\text{X-ray}}$ = X-ray density, N_A = Avogadro number, M = molar mass, and V_{cell} = volume of the unit cell.

The calculated values of X-ray densities of series samples also show a decrease with the increase of Bi^{2+} contents. The mass density/bulk density of the samples was determined by the following equation [26,27].

$$\rho_m = \frac{m}{\pi r^2 h} \quad (4)$$

where, m = mass of the pellet, ρ_m = bulk density, r = radius of the pellet and h = thickness of the pellet.

The calculated values X-ray densities of samples are given in Table (1), which are higher as compared to those of bulk densities indicating the presence of pores in the samples. Further, it was confirmed by calculating the porosity due to the substitution of relatively larger Bi^{2+} ions in place of smaller ions. The samples percentage porosity was determined by the following equation and given in Table 1.

$$P = \left(1 - \frac{\rho_m}{\rho_x}\right) \times 100 \quad (5)$$

where, P = Porosity, ρ_x = X-ray density and ρ_m = bulk density

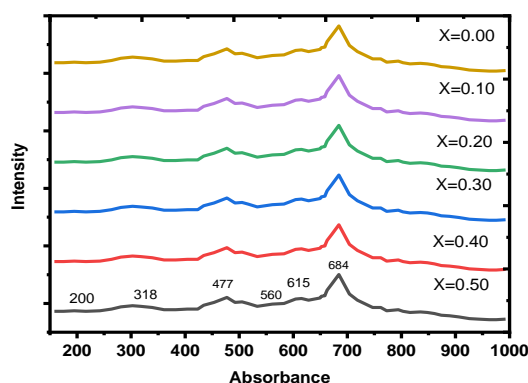
Table 1 shows the measured lattice constant, density, and porosity for six samples [28]. It indicates that an increase in the values with the increase of ' Bi ' contents. As the ionic radius of ' Bi^{2+} ' is greater than that of the Fe^{3+} , Mn^{2+} and Ni^{2+} , the increase in lattice constant is expected by increasing the contents of Bi^{2+} dopant.

Table 1. Physical and Lattice Parameters of Synthesized $\text{Bi}_{0.6-x}\text{Mn}_{0.5}\text{Ni}_{0.5}\text{Fe}_2\text{O}_4$ nanoparticles.

Compositions	Lattice constant (\AA)	Volume (\AA^3)	Crystallite size (nm)	X-ray density (g cm^{-3})	Bulk density (g cm^{-3})	Porosity
$\text{Mn}_{0.5}\text{Ni}_{0.5}\text{Fe}_2\text{O}_4$	8.3485	581.86	26.08	5.329	3.342	37.28
$\text{Bi}_{0.1}\text{Mn}_{0.5}\text{Ni}_{0.5}\text{Fe}_2\text{O}_4$	8.4214	597.25	28.04	5.448	3.544	34.94
$\text{Bi}_{0.2}\text{Mn}_{0.5}\text{Ni}_{0.5}\text{Fe}_2\text{O}_4$	8.4223	597.43	28.56	5.579	3.546	36.44
$\text{Bi}_{0.3}\text{Mn}_{0.5}\text{Ni}_{0.5}\text{Fe}_2\text{O}_4$	8.4225	597.56	31.27	5.580	3.577	35.89
$\text{Bi}_{0.4}\text{Mn}_{0.5}\text{Ni}_{0.5}\text{Fe}_2\text{O}_4$	8.4229	597.56	32.70	5.582	3.646	34.68
$\text{Bi}_{0.5}\text{Mn}_{0.5}\text{Ni}_{0.5}\text{Fe}_2\text{O}_4$	8.4298	599.04	34.64	5.589	3.789	32.12

3.2. Raman spectroscopy

As per literature, the Raman Spectroscopy suggests five Raman active bands A_{1g} , E_g , and three belong to T_{2g} modes [29]. The room temperature Raman spectra of $\text{Bi}_{0.6-x}\text{Mn}_{0.5}\text{Ni}_{0.5}\text{Fe}_2\text{O}_4$ (where “x” in the formula varies from 0.0-0.50) nanomaterials were achieved as shown in Fig. 2. In these spectra shows five peaks are at 200, 318, 477, 560, and 684 cm^{-1} as appeared in the range of 0-1000 cm^{-1} . The typical peak of spinel ferrite appears at 684 cm^{-1} which is assigned to A_{1g} mode and corresponds to the symmetric stretch of oxygen ions along with Fe-O bonds at the tetrahedral sites [30]. The other two peaks at 318 cm^{-1} and 477 cm^{-1} are assigned to E_g and T_{2g} (2) modes which related to the symmetric bending of oxygen ions with respect to Fe [31].

Fig. 2. Raman spectrums series of $\text{Bi}_{0.6-x}\text{Mn}_{0.5}\text{Ni}_{0.5}\text{Fe}_2\text{O}_4$ nanoparticles.

Whereas, the other two peaks at 200 cm^{-1} and 560 cm^{-1} represent $T_{2g}(1)$ and $T_{2g}(3)$ modes which correspond to the translational movement of the entire $\text{Bi}_{0.6-x}\text{Mn}_{0.5}\text{Ni}_{0.5}\text{Fe}_2\text{O}_4$ tetrahedron and the asymmetric bending of oxygen ions with respect to Fe [31, 32]. The appearance of all these peaks in the Raman spectrum at appropriate energies confirms the successful formation of $\text{Bi}_{0.6-x}\text{Mn}_{0.5}\text{Ni}_{0.5}\text{Fe}_2\text{O}_4$ cubic nanoparticles.

3.3. Morphological analysis

The results of SEM and EDX give information about the structural morphology of the microstructures beside the sizes, shapes, and distributions, along with their chemical compositions in the microstructures. The energy dispersive spectroscopy (EDS) is used to get information about the chemical composition of the $\text{Bi}_{0.6-x}\text{Mn}_{0.5}\text{Ni}_{0.5}\text{Fe}_2\text{O}_4$ nanoparticles. The EDS spectrum depicts the presence of oxygen, Bismuth, cobalt, nickel, and Iron as can be observed of the peaks in Fig. 4. The exact composition of the synthesized ferrite nanomaterial indicated in the results of the

EDS analysis is shown in Table (2). Results show the exact composition of the synthesized ferrite nanomaterial, thus confirming the purity of the synthesized ferrite

nanomaterials. The SEM micrographs of $\text{Bi}_{0.6-x}\text{Mn}_{0.5}\text{Ni}_{0.5}\text{Fe}_2\text{O}_4$ as shown in Fig. 3a give information that the synthesized nanoparticles are spherical and have grown in a leaflike pattern.

Table 2 Results of EDS analysis of $\text{Bi}_{0.6-x}\text{Mn}_{0.5}\text{Ni}_{0.5}\text{Fe}_2\text{O}_4$ nanoparticles.

Sample	Vale of X	Bismuth wt %	Nickel wt %	Manganese wt %	Iron wt %	oxygen wt %
$\text{Bi}_{0.6-x}\text{Mn}_{0.5}\text{Ni}_{0.5}\text{Fe}_2\text{O}_4$	0.0	0.0	19.84	19.32	41.08	20.50
$\text{Bi}_{0.6-x}\text{Mn}_{0.5}\text{Ni}_{0.5}\text{Fe}_2\text{O}_4$	0.5	9.39	18.84	16.32	39.08	20.30

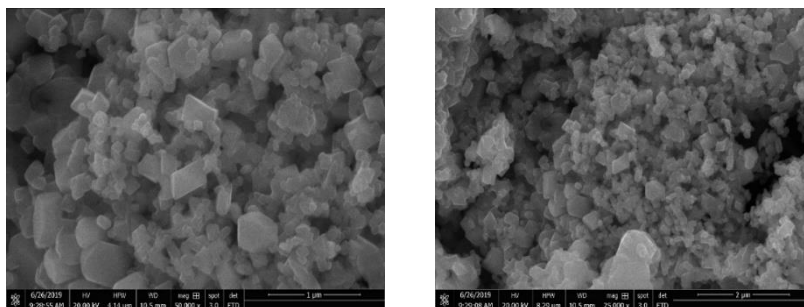


Fig.3. (a) Showing the SEM micrographs of $\text{Mn}_{0.5}\text{Ni}_{0.5}\text{Fe}_2\text{O}_4$ (b) Showing the SEM of $\text{Bi}_{0.5}\text{Mn}_{0.5}\text{Ni}_{0.5}\text{Fe}_2\text{O}_4$.

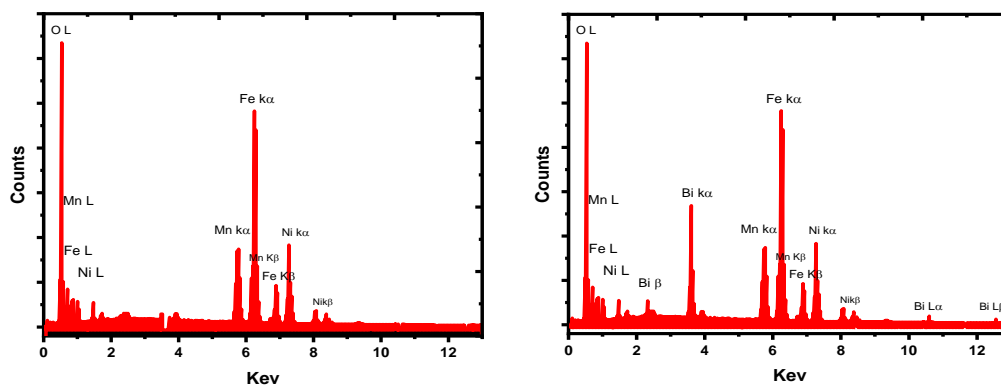


Fig. 4. (a) Results of the EDS of $\text{Mn}_{0.5}\text{Ni}_{0.5}\text{Fe}_2\text{O}_4$ (b) Results of the EDS of $\text{Bi}_{0.5}\text{Mn}_{0.5}\text{Ni}_{0.5}\text{Fe}_2\text{O}_4$.

3.4. Thermal analysis

The samples were also subjected to both TGA and DTA by heating the samples of $\text{Bi}_{0.5}\text{Mn}_{0.5}\text{Ni}_{0.5}\text{Fe}_2\text{O}_4$ nano-ferrite up to $1000\text{ }^\circ\text{C}$ by using a heating rate of $10\text{ }^\circ\text{C}$ per minute in the air. The results of TGA/DTA curves give information about mass loss or gain during decomposition or oxidation process. The results depicted in Fig. 5 a, b and c illustrates the typical behavior of TGA, and DTA curves of the samples $\text{Bi}_{0.5}\text{Mn}_{0.5}\text{Ni}_{0.5}\text{Fe}_2\text{O}_4$ nano-ferrites. At the initial stage weight losses are observed up to $100\text{ }^\circ\text{C}$ that corresponds to the evaporation of water contents absorbed by the samples during storage. The identified three regions of weight loss at $410\text{--}530\text{ }^\circ\text{C}$ temperature corresponds to endothermic peaks whereas the second weight loss in the same temperature regions ($410\text{--}530\text{ }^\circ\text{C}$) corresponds to the decomposition of iron oxide Fe_2O_3 and MnO_2 . Finally, at a higher temperature, the TGA curve became more flattened, indicating a single-phase formation. The results of the DTA curve for $\text{Bi}_{0.5}\text{Mn}_{0.5}\text{Ni}_{0.5}\text{Fe}_2\text{O}_4$ indicated two sharp peaks at $477\text{ }^\circ\text{C}$ and $489\text{ }^\circ\text{C}$ which corresponds to the exothermic nature of the reaction. Therefore, the weight loss at these temperatures is about $0.68\% / ^\circ\text{C}$ and $0.95\% / ^\circ\text{C}$, respectively.

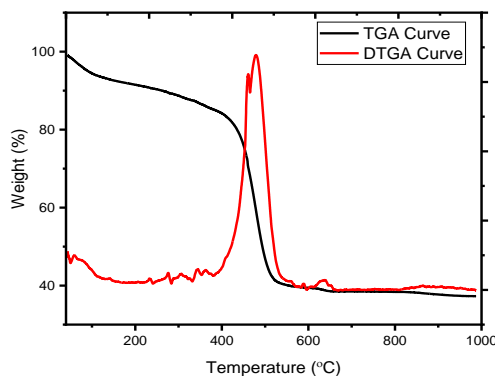


Fig. 5. Results of the TGA and DTA curves of $\text{Bi}_{0.5}\text{Mn}_{0.5}\text{Ni}_{0.5}\text{Fe}_2\text{O}_4$.

3.5. Dielectric properties

The LCR meter is used for dielectric measurements of palletted samples of $\text{Bi}_{0.5}\text{Mn}_{0.5}\text{Ni}_{0.5}\text{Fe}_2\text{O}_4$ nano-ferrite. The palletted samples have dimensions 12mm in diameter and the thickness range 0.5-2 mm were prepared using a hydraulic pressing technique by applying a pressure of 120-150 Kg/cm^2 tones.

The dielectric constant of the samples was determined by varying the range of frequency from 50 Hz to 10MHz. The phenomenon of dielectric behavior of ferrite materials is well explained by Koop's and Maxwell Wagner's [33] in which the dielectric constant could be determined by using the equation (6) as given below:

$$\hat{\epsilon} = \frac{Cd}{\epsilon^0 A} \quad (6)$$

where, A = area of the pallet, C = capacitance, d = thickness, ϵ_0 = absolute permittivity.

The dielectric properties of $\text{Bi}_{0.5}\text{Mn}_{0.5}\text{Ni}_{0.5}\text{Fe}_2\text{O}_4$ nano-ferrite are affected by the variation of ' Bi^{2+} ' concentration as can be seen in the results depicted in Fig. 6 that the dielectric permittivity diminishes with the increment in frequency. The reason with the rise in the concentration of Bi^{2+} causes a diminishes within the concentration of Ni^{+2} and Mn^{2+} particles. As a result, the Fe^{+2} particles ended up with fewer numbers of gaps for electron bouncing. Subsequently, the build-up of charges over the grain boundaries causes an increase in resistance [34]. That's why the decrease in electrical permittivity is observed with an increase in the concentration of ' Bi^{2+} ' ions.

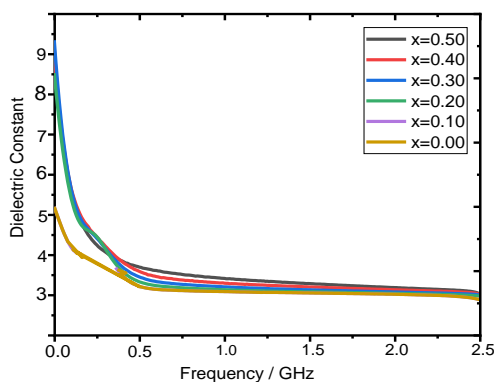


Fig. 6. Results of the dielectric permittivity of the synthesized series of $\text{Bi}_{0.6-x}\text{Mn}_{0.5}\text{Ni}_{0.5}\text{Fe}_2\text{O}_4$.

3.6. Magnetic properties

Fig. 7 shows the results of magnetic hysteresis curves of $\text{Bi}_{0.6-x}\text{Mn}_{0.5}\text{Ni}_{0.5}\text{Fe}_2\text{O}_4$ nanoparticles (where $x=0.0$ to 0.50) which were recorded under the applied magnetic field range 10-100 kOe at room temperature. It can be deduced from hysteresis curves in Fig. 7 that 'Mn' and 'Ni' ferrite nanoparticles with smaller crystallite and grain size are superparamagnetic than Bi, Mn and Ni ferrite nanoparticles are poor ferrimagnetic with coercive fields of 2 and 25 Oe, respectively. It is known that below the single domain limit, the coercive field reduced with a decrease in the particle size and approaches 0 Oe at the superparamagnetic restrain. The specific saturation magnetization, calculated by the intercept of magnetization versus $1/H$, was found to vary between 8 and 21 emu/g. The calculated values are much lower than that of the bulk counterpart (82 emus/g for Ni Mn ferrites).

The Magnetic performance of our synthesized nanocrystals series measured by VSM can be ascribed due to the competition of ferromagnetic particles such as ' Fe^{3+} ', ' Ni^{2+} ' ions, paramagnetic particles ' Mn^{2+} ' ions and non-magnetic particles ' Bi^{2+} ' ions within the inhabitation of the tetrahedral and octahedral destinations.

The decrease in the saturation magnetization of $\text{Mn}_{0.5}\text{Ni}_{0.5}\text{Fe}_2\text{O}_4$ can be described due to the absence of the ' Ni^{2+} ' ions as ferromagnetic ions and paramagnetic ' Mn^{2+} ' ions by the habitation of Bi^{2+} ions with zero magnetic moment in all tetrahedral sites, and also replacing the ' Fe^{3+} ' ions in the octahedral sites. Subsequently, ' Fe^{3+} ' ions in the octahedral sites could not significantly interact with each other, hence the magnetization of $\text{Bi}_{0.6-x}\text{Mn}_{0.5}\text{Ni}_{0.5}\text{Fe}_2\text{O}_4$ nanocrystals is decreased. Also, with the increase in the Bi^{2+} content from $x=0.1$ to $x=0.5$, a small reduction is observed in the saturation magnetization.

Since the coercivity of a magnetic material is a measure of its magneto-crystalline anisotropy, the small nanoparticles, which have close to zero coercivity and no remanence become single domain with little anisotropy energy [35]. This is a characteristic of superparamagnetic nanocrystals. The coercivity of the synthesized $\text{Bi}_{0.6-x}\text{Mn}_{0.5}\text{Ni}_{0.5}\text{Fe}_2\text{O}_4$ nanocrystals series has been obtained from Fig. 7 are near to zero. Hence, these nanocrystals show superparamagnetic behavior at room temperature. Such properties make these materials favorable for wide applications in engineering, such as drugs delivery [36], bio-separation [37] and magnetic refrigeration frameworks[38].

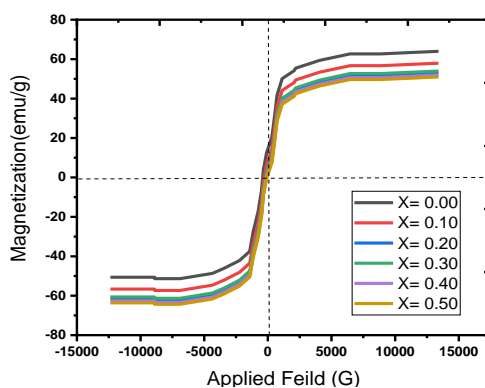


Fig. 7. Results of the Magnetic Hysteresis curves of the synthesized series of $\text{Bi}_{0.6-x}\text{Mn}_{0.5}\text{Ni}_{0.5}\text{Fe}_2\text{O}_4$ nanoparticles.

4. Conclusion

In this study, the co-precipitation technique is successfully used for the synthesis of nanoparticles

$\text{Bi}_{0.6-x}\text{Mn}_{0.5}\text{Ni}_{0.5}\text{Fe}_2\text{O}_4$ series (where $x=0.0$ to 0.50) which exhibits a spinel structure with varying sizes from 25-35nm. The spinel cubic structure is confirmed by the result of the XRD patterns. The synthesized $\text{Bi}_{0.6-x}\text{Mn}_{0.5}\text{Ni}_{0.5}\text{Fe}_2\text{O}_4$ nanoparticles series have a high level of crystallinity and porosity. The Raman spectra of $\text{Bi}_{0.5}\text{Mn}_{0.5}\text{Ni}_{0.5}\text{Fe}_2\text{O}_4$ nanoparticles series confirm

the five Raman modes and indicates the distribution cations and anions in octahedral and tetrahedral sublattices in the synthesized samples. Moreover, thermal analysis studies showed the stability of the synthesized $\text{Bi}_{0.5}\text{Mn}_{0.5}\text{Ni}_{0.5}\text{Fe}_2\text{O}_4$ nanoparticles at high temperatures. The dielectric studies show that polarization in the samples is associated with the conduction process due to the hopping mechanism. The dielectric permittivity diminishes with the rise in frequency due to the addition of Bi^{2+} ions in the sample's series. In the prepared samples of the synthesized nanoparticles, the magnetic hysteresis curves showed a pronounced reduction in saturation magnetization with the increase in the Bi concentration, as the addition of ' Bi^{2+} ' ions replaces the other ions within the framework of $\text{Mn}_{0.5}\text{Ni}_{0.5}\text{Fe}_2\text{O}_4$. This replacement caused the randomization of particles spins in the nanoparticles, where the number of particles on the surface is high compared to that within the volume. The noncollinear spin arrangement on the surface of $\text{Bi}_{0.6-x}\text{Mn}_{0.5}\text{Ni}_{0.5}\text{Fe}_2\text{O}_4$ nanoparticles cause size dependence saturation of magnetization.

Acknowledgments

The authors would like to thank the Ministry of Higher Education Commission of Pakistan to provide support for research activities at IUB Baghdad Road Bahawalpur.

References

- [1] G. Korotcenkov, *Chemical Sensors Fundamentals of Sensing Materials*, Momentum Press p. 370, 2010.
- [2] M. Azhar Khan, M. Sabir, A. Mahmood, M. Asghar, K. Mahmood, M. Afzal Khan, I. Ahmad, M. Sher, M. Farooq Warsi, *J. Magn. Magn. Mater.* **360**, 188 (2014).
- [3] J. A. Toledo, M. A. Valenzuela, P. Bosch, H. Armendáriz, A. Montoya, N. Nava, A. Vázquez, *Appl. Catal. A: Gen.* **198**, 235 (2000).
- [4] C. V. Gangatharan Sathishkumar, Kandasamy Sivakumar, *Mater. Sci. Appl.* **1**, 19 (2010).
- [5] M. Y. Lodhi, K. Mahmood, A. Mahmood, H. Malik, M. F. Warsi, I. Shakir, M. Asghar, M. A. Khan, *Curr. Appl. Phys.* **14**, 716 (2014).
- [6] M. N. Ashiq, M. F. Ehsan, M. J. Iqbal, I. H. Gul, *J. Alloy. Compd.* **509**, 5119 (2011).
- [7] H. Malik, A. Mahmood, K. Mahmood, M. Y. Lodhi, M.F. Warsi, I. Shakir, H. Wahab, M. Asghar, M. A. Khan, *Ceram. Int.* **40**, 9439 (2014).
- [8] M. M. Rashad, E. M. Elsayed, M. M. Moharam, R. M. Abou-Shahba, A. E. Saba, *J. Alloy. Compd.* **486**, 759 (2009).
- [9] P. Priyadharsini, A. Pradeep, P. S. Rao, G. Chandrasekaran, *Mater. Chem. Phys.* **116**, 207 (2009).
- [10] M. Hua, S. Zhang, B. Pan, W. Zhang, L. Lv, Q. Zhang, *J. Hazard. Mater.* **211–212**, 317 (2012).
- [11] L. Wanga, J. Li, Y. Wang, L. Zhao, Q. Jiang, *Chem. Eng. J.* **181–182**, 72 (2012).
- [12] P. V. Nidheesh, R. Gandhimathi, S. T. Ramesh, *Environ. Sci. Pollut. Res.* **20**, 2099 (2013).
- [13] E. Casbeer, V. K. Sharma, X.-Z. Li, *Sep. Purif. Technol.* **87**, 1 (2012).
- [14] A. Goyal, S. Bansal, S. Singhal, *Int. J. Hydrogen Energy* **39**, 4895 (2014).
- [15] L. Huang, G. Su, A. Zhang, Y. Shi, C. Xia, H. Lu, L. Li, S. Liu, M. Zheng, *J. Hazard. Mater.* **261**, 451 (2013).
- [16] W. Zhang, B. Quan, C. Lee, S. K. Park, X. Li, E. Choi, G. Diao, Y. Piao, *ACS Appl. Mater. Interfaces* **7**(4), 2404 (2015).
- [17] R. Ali, A. Mahmood, M. A. Khan, A. H. Chughtai, M. Shahid, I. Shakir, M. F. Warsi, *J. Alloy. Compd.* **584**, 363 (2014).
- [18] M. M. Mallapur, P. A. Shaikh, R. C. Kambale, H. V. Jamadar, P. U. Mahamuni, B. K. Chougule, *J. Alloy. Compd.* **479**, 797 (2009).
- [19] K. Mohit, V. R. Gupta, N. Gupta, S. K. Rout, *Ceram. Int.* **40**, 1575 (2014).
- [20] P. P. Sarangi, S. R. Vadera, M. K. Patra, N. N. Ghosh, *Powder Technol.* **203**, 348 (2010).
- [21] T. J. Shinde, A. B. Gadkari, P. N. Vasambekar, *J. Magn. Magn. Mater.* **333**, 152 (2013).

- [22] K. Velmurugan, V. S. K. Venkatachalapathy, S. Sendhilnathan, *Mater. Res.* **13**, 299 (2010).
- [23] M. A. Khan, M. U. Islam, M. Ishaque, I. Z. Rahman, *Ceram. Int.* **37**, 2519 (2011).
- [24] M. A. Khan, M. U. Islam, M. Ishaque, I. Z. Rahman, A. Genson, S. Hampshire, *Mater. Charact.* **60**, 73 (2009).
- [25] I. H. Gul, A. Z. Abbasi, F. Amin, M. Anis-ur-Rehman, A. Maqsood, *J. Magn. Magn. Mater.* **311**, 494 (2007).
- [26] A. Mahmood, M. F. Warsi, M. N. Ashiq, M. Ishaq, *J. Magn. Magn. Mater.* **327**, 64 (2013).
- [27] R. D. Waldron, *Phys. Rev.* **99**, 1727 (1955).
- [28] H. Kumar, J. P. Singh, R. C. Srivastava, P. Negi, H. M. Agrawal, K. Asokan, *J. Nanosci.* **2014**, 10 (2014).
- [29] A. Maqsood, K. Khan, M. Anis-ur-Rehman, M. A. Malik, *J. Alloy. Compd.* **509**, 7493 (2011).
- [30] M. Shahid, L. Jingling, Z. Ali, I. Shakir, M. F. Warsi, R. Parveen, M. Nadeem, *Mater. Chem. Phys.* **139**, 566 (2013).
- [31] S. R. Liu, D. H. Ji, J. Xu, Z. Z. Li, G. D. Tang, R. R. Bian, W. H. Qi, Z. F. Shang, X. Y. Zhang, *J. Alloy. Compd.* **581**, 616 (2013).
- [32] C. N. Chinnasamy, A. Narayanasamy, N. Ponpandian, K. Chattopadhyay, K. Shinoda, B. Jeyadevan, K. Tohji, K. Nakatsuka, T. Furubayashi, I. Nakatani, *Phys. Rev. B* **63**, 184108 (2001).
- [33] M. N. Ashiq, M. Javed Iqbal, I. Hussain Gul, *J. Magn. Magn. Mater.* **323**, 259 (2011).
- [34] C. G. Koops, *Phys. Rev.* **83**, 121 (1951).
- [32] Y. Zheng, Z. Li, J. Xu, T. Wang, X. Liu, X. Duan, Y. Ma, Y. Zhou, C. Pei, *Nano Energy* **20**, 94 (2016).
- [35] J. Chand, S. Verma, P. Kumar, M. Singh, *Int.J. Theor. Appl. Sci.* **III**(2), 2 (2011).
- [36] Z. Anwar, M. Azhar Khan, I. Ali, M. Sher, I. Shakir, M. Sarfraz, M. F. Warsi, *J. Ovonic Res.* **10**, 265 (2014).
- [37] R. Peelamedu, C. Grimes, D. Agrawal, R. Roy, P. Yadoji, *J. Mater. Res.* **18**, 2292 (2003).
- [38] M. J. Iqbal, M. N. Ashiq, *Chem. Eng. J.* **136**, 383 (2008).